

Enhanced thermoelectric properties of the topological phase of monolayer HfC

Wenlai Mu(母文来), Nisar Muhammad(穆罕默德·尼萨), Baojuan Dong(董宝娟), Nguyen Tuan Hung(阮俊兴), Huaihong Guo(郭怀红), Riichiro Saito(斋藤理一郎), Weijiang Gong(公卫江), Teng Yang(杨腾), and Zhidong Zhang(张志东)

Citation : Chin. Phys. B, 2025, 34 (**5**): 057301. DOI: 10.1088/1674-1056/adbd17
http://cpb.iphy.ac.cn; http://iopscience.iop.org/cpb

What follows is a list of articles you may be interested in

First principles prediction of the valley Hall effect in ScBrCl monolayer

Xiang Yu(于翔), Ping Li(李萍), and Chang-Wen Zhang(张昌文)
Chin. Phys. B, 2025, 34 (**4**): 047305. DOI: 10.1088/1674-1056/adbacb

Electronic structure and carrier mobility of BSb nanotubes

Lantian Xue(薛岚天), Chennan Song(宋晨楠), Miaomiao Jian(见苗苗), Qiang Xu(许强), Yuhao Fu(付钰豪), Pengyue Gao(高朋越), and Yu Xie(谢禹)
Chin. Phys. B, 2025, 34 (**3**): 037304. DOI: 10.1088/1674-1056/adacd3

Intrinsic valley-polarized quantum anomalous Hall effect in a two-dimensional germanene/MnI_2 van der Waals heterostructure

Xiao-Jing Dong(董晓晶) and Chang-Wen Zhang(张昌文)
Chin. Phys. B, 2024, 33 (**7**): 077303. DOI: 10.1088/1674-1056/ad4bbd

Light-modulated graphene-based φ_0 Josephson junction and $-\varphi_0$ to φ_0 transition

Renxiang Cheng(程任翔), Miao Yu(于苗), Hong Wang(汪洪), Deliang Cao(曹德亮), Xingao Li(李兴鳌), Fenghua Qi(戚凤华), and Xingfei Zhou(周兴飞)
Chin. Phys. B, 2024, 33 (**2**): 027302. DOI: 10.1088/1674-1056/ad04c5

Thermoelectric effects and topological insulators

Yong Xu(徐勇)
Chin. Phys. B, 2016, 25 (**11**): 117309. DOI: 10.1088/1674-1056/25/11/117309

Enhanced thermoelectric properties of the topological phase of monolayer HfC

Wenlai Mu(母文来)[1], Nisar Muhammad(穆罕默德·尼萨)[2], Baojuan Dong(董宝娟)[3,4,5], Nguyen Tuan Hung(阮俊兴)[6,†], Huaihong Guo(郭怀红)[7,‡], Riichiro Saito(斎藤理一郎)[8], Weijiang Gong(公卫江)[9], Teng Yang(杨腾)[1,3,§], and Zhidong Zhang(张志东)[1]

[1] *Shenyang National Laboratory for Materials Science, Institute of Metal Research, Chinese Academy of Sciences, School of Materials Science and Engineering, University of Science and Technology of China, Shenyang* 110016, *China*
[2] *Hefei National Laboratory for Physical Sciences at Microscale and Department of Physics, University of Science and Technology of China, Hefei* 230026, *China*
[3] *Liaoning Academy of Materials, Shenyang* 110167, *China*
[4] *State Key Laboratory of Quantum Optics and Quantum Optics Devices, Institute of Opto-Electronics, Shanxi University, Taiyuan* 030006, *China*
[5] *Collaborative Innovation Center of Extreme Optics, Shanxi University, Taiyuan* 030006, *China*
[6] *Frontier Research Institute for Interdisciplinary Sciences, Tohoku University, Sendai* 980-8578, *Japan*
[7] *College of Sciences, Liaoning Petrochemical University, Fushun* 113001, *China*
[8] *Department of Physics, Tohoku University, Sendai* 980-8578, *Japan*
[9] *College of Sciences, Northeastern University, Shenyang* 110819, *China*

(Received 10 January 2025; revised manuscript received 3 March 2025; accepted manuscript online 6 March 2025)

Thermoelectric properties of a topological insulator, monolayer HfC, are calculated using first-principles calculation, which accounts for the two contributions from edge and bulk states. By applying strain up to 8% along the a axis, the monolayer HfC shows the topological phase while it is in a non-topological state without strain. The figure of merit, ZT, for the topological phase becomes two-ordered magnitude larger ($ZT \sim 2$) because of larger electric conductivity than that of the non-topological phase due to edge current. The total Seebeck coefficient S, and ZT have maximum values when the chemical potential is located at the highest energy of the edge state. The peak of ZT comes from the fact that the product of divergent S and quickly-decreasing electric conductivity above the highest energy of the edge state. We further optimize S and ZT by changing the sample size and temperature.

Keywords: anomalous Seebeck effect, *ab initio* calculations, edge state, hafnium carbide, thermoelectric, Z_2 topological insulator

PACS: 73.50.Lw, 31.15.A–

DOI: 10.1088/1674-1056/adbd17 **CSTR:** 32038.14.CPB.adbd17

1. Introduction

A thermoelectric (TE) device that can directly convert heat energy into electrical energy is evaluated by the dimensionless figure of merit $ZT = \sigma S^2 T/(\kappa_e + \kappa_p)$, where κ_e and κ_l are the thermal conductivity contributed by electrons and phonons, respectively, T is the average temperature in device, σ is the electrical conductivity, and S is the Seebeck coefficient.[1] A higher ZT value leads to a larger TE efficiency of the energy conversion, in which ZT around two at working temperature is needed for practical applications.[2] Since ZT is proportional to the square of S, finding the material (usually semiconductor materials) with a large value of S while still maintaining good σ is important to the enhancement of thermoelectric performance.

To obtain a large value of the Seebeck coefficient with concomitant good electrical conductivity, several strategies have been introduced, such as using narrow band-gap semiconductors (0.5–1.0 eV) with multiple energy valleys (or so-called band convergence),[3,4] low-dimensional semiconductors with quantum confinement effect.[5–9] In a semiconductor material, one finds a large Seebeck coefficient when the chemical potential is located at the bottom of the conduction band. But this is always accompanied by poor electrical conductivity. In the case of topological material, however, the edge states gives a large electrical conductivity compared with that of intrinsic semiconductor.[10] This situation modifies the concept of thermoelectricity for topological phase. Here we show in the case of topological material, the peak of Seebeck coefficient appears at much higher energy from the bottom of conduction band at which the nature of edge states start to disappear.

A topological material, for example topological insulator (TI), exhibits a bulk band gap and robust gapless edge states with Dirac–Fermion-like linear dispersion.[11–14] There-

†Corresponding author. E-mail: nguyen.tuan.hung.e4@tohoku.ac.jp
‡Corresponding author. E-mail: hhguo@alum.imr.ac.cn
§Corresponding author. E-mail: yanghaiteng@msn.com

© 2025 Chinese Physical Society and IOP Publishing Ltd. All rights, including for text and data mining, AI training, and similar technologies, are reserved.

fore, the TIs provide two different transport channels; one is from the edge states and the other from the (conventional) semiconducting bulk inner part, both of which could help to obtain large S and high σ.[15] Unlike a metal in which a gapless Dirac band has a very small S value due to the cancellation effect from electron–hole contributions to the Seebeck coefficient,[16] the gapless edge states of the TIs have a large S value with anomalous signs when the Fermi level is located around the bulk band boundaries, the so-called anomalous Seebeck effect (ASE).[15] Among the previous theoretical studies,[15,17,18] bulk and edge states were assumed to be isolated in energy range, i.e., the edge states are mainly located inside the bulk band gap. Thus, one can treat the scattering rates (or the relaxation time) separately for bulk and edge states, which are usually taken as constant. However, this approximation may lead to a loss of information regarding the interference between the bulk and edge states. For instance, the band structure of TIs often exhibits overlap between the bulk and edge bands.[19] This interference effect on the TE properties has not been well understood. On the other hand, a direct comparison of TE properties between the trivial and non-trivial topological phases in a single material is crucial for gaining a better understanding of the topological-state-induced TE enhancement. It has recently been predicted and reported that the HfC monolayer has a strain-induced topological phase transformation.[20] Moreover, its topological edge states have an obvious overlap in energy with bulk states. Thus, HfC monolayer is a good example not only to explore the mechanism of ASE but also to reveal the TE enhancement due to topological phase transition.

In this work, the thermoelectric (TE) performance of the two-dimensional topological insulator (2D TI) is investigated in the HfC monolayer, which has both the trivial and non-trivial TI phases. By using the dual-channel model, in which scattering rates are evaluated within the deformation potential theory, we discuss the optimized TE performance due to the separate contributions of both the normal Seebeck effect (NSE) and the ASE by the bulk and edge states, respectively.

2. Results and discussion

2.1. Electronic band structure

The HfC monolayer as a rectangle lattice has lattice constants of $a = 3.78$ Å and $b = 4.51$ Å with two carbon atoms and two hafnium atoms in the unit cell, as illustrated in Fig. 1(a). A vacuum layer in thickness of 20 Å was used to avoid interlayer interaction. The study by Zhou *et al.*[20] showed that the HfC monolayer has a topological phase transition under certain unidirectional strains. Thus, we selected two typical atomic structures for comparison, one with zero strain and the other with -8% strain along a direction. The -8% strain was selected in this study due to the largest band gap (~ 0.1 eV) for the topological phase of the HfC monolayer.[20] For verifying the topological phase, we calculated the Wilson loop of the Wannier centers of the strained structure, as represented in Fig. A3 in Appendix A, which shows the Z_2 topological characteristic. The fully relaxed structures exhibit dynamical stability, as shown in Fig. A1, and can sustain temperatures up to 1000 K.

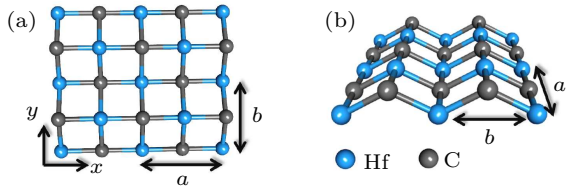


Fig. 1. Lattice structure of monolayer hafnium carbide (HfC) with (a) top view and (b) side view, in which the blue ball denotes the hafnium atom, while the black ball denotes the carbon atom.

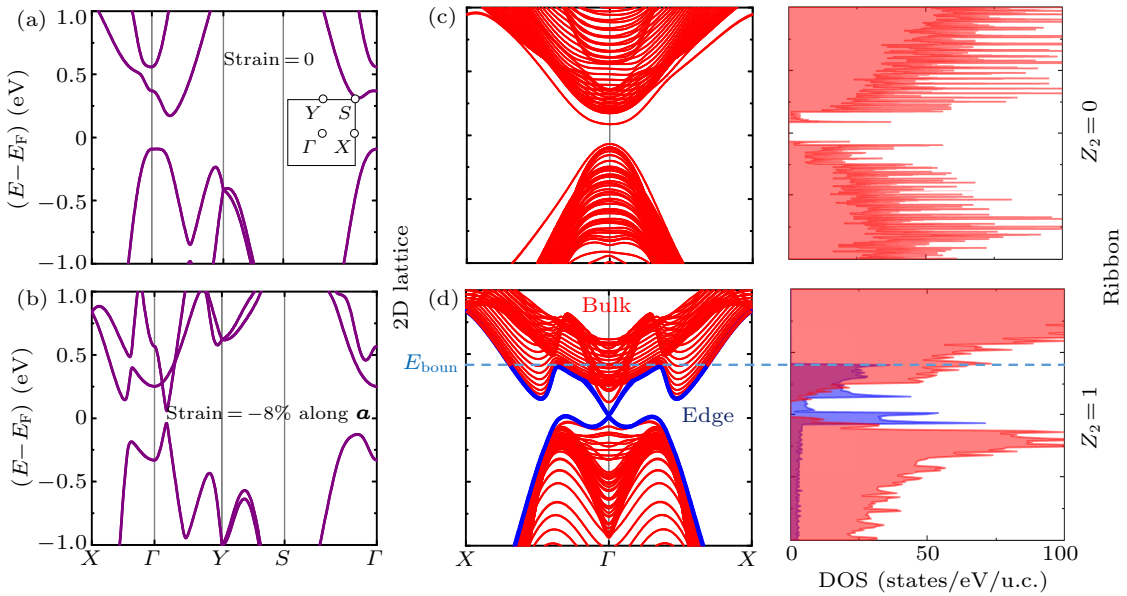


Fig. 2. Electronic band structure of (a) topological trivial phase with $Z_2 = 0$ and (b) topological non-trivial phase with $Z_2 = 1$. The electronic band structure with the density of states (DOS) in the ribbon phases in panels (c) and (d) corresponds to that in the bulk phases in panels (a) and (b), respectively. In panel (d), the bulk and edge parts were marked in red and blue colors, respectively.

The calculated electronic band structures of the HfC monolayer under two strains are illustrated in Figs. 2(a) and 2(b). The result derived from the tight-binding model of the WANNIER90 code fits well with the density functional theory (DFT) calculation, as shown in Fig. A2. To manifest the function of the edge states, we shifted our focus from a two-dimensional (2D) monolayer to a one-dimensional (1D) HfC nanoribbon. The calculated electronic band structures and density of states (DOS) of both unstrained and unidirectionally strained ribbons are given in Figs. 2(c) and 2(d). The unstrained 1D and 2D structures are both semiconducting with an indirect band gap around 0.3 eV and $Z_2 = 0$ from Figs. 2(a) and 2(c), while the strained structures in Figs. 2(b) and 2(d) were confirmed to be $Z_2 = 1$ TI based on the calculated surface DOS and the Wilson loop (shown in Fig. A2).

From the electronic band of the TI phase of the HfC nanoribbon in Fig. 2(d), the topological edge states can also be observed and are highlighted in blue in accordance with the results of the surface DOS of the HfC monolayer in Fig. A2. Compared with conventional boundary states with Dirac-type linear dispersion relation,[15] the edge states here possess several energy valleys in the energy window of interest. These edge band characteristics may induce additional semi-metal-like Seebeck coefficient peaks. The electronic band and DOS of the trivial phase of the HfC nanoribbon are also given in Fig. 2(c) for comparisons.

To note that the topological edge state is denoted as *e* and the bulk one denoted as *b*. The TI phase of the system has a gapless band from -1.00 eV to 0.40 eV with coexisting *e* and *b* states.

2.2. Transport and thermoelectric properties

First, we compare TE properties between the TI phase ($Z_2 = 1$) and the trivial phase ($Z_2 = 0$), as demonstrated in Fig. 3. For the trivial phase on the left-hand side of Fig. 3(a), the system shows its characteristic of a narrow-band gap semiconductor, in which electrical conductivity has a V-shaped curve. For the TI phase on the right-hand side, the electrical conductivity spectrum is no longer a V-shaped curve, and a series of conductivity plateaus emerge. The relaxation time of the systems is calculated via the deformation potential theory,[21] and more details are given in Appendix A2. Although the relaxation time of the trivial phase at the bulk boundary $\tau_{0p} = 159.55/\sqrt{T}$ and $\tau_{0n} = 161.92/\sqrt{T}$ (in the unit of fs, where T denotes temperature) is higher by about an order of magnitude than that of the bulk state in the TI phase $\tau_{1p} = 7.45/\sqrt{T}$ and $\tau_{1n} = 21.19/\sqrt{T}$, the electrical conductivity σ of TI phase is still much higher (by almost 3 orders of magnitude) than that of trivial phase due to the high electron mobility of topological edge states. High σ usually comes along with high electronic thermal conductivity κ_e. That is why the TI phase has total thermal conductivity κ ($= \kappa_e + \kappa_l$) dominated by electron contribution (κ_e), as seen from the similar chemical potential μ dependence of κ as σ on the right panel of Figs. 3(a) and 3(b). As a comparison, the total thermal conductivity κ of the trivial phase is dominated by phonon contribution (κ_l), as seen from the chemical potential independence of κ on the left panel of Fig. 3(b). κ_l plays different roles in κ of the two phases, which is directly seen from the calculated lattice thermal conductivity in Fig. A1(b). The TI phase has a lower phonon lifetime (mainly due to stronger phonon anharmonicity) than that of the trivial phase, resulting in a much lower κ_l in the TI phase (i.e., $\kappa_l = 2.06$ W·m^{-1}·K^{-1} and 14.60 W·m^{-1}·K^{-1} for the TI and trivial phase, respectively, at 300 K). To note that, due to the large unit cell of the 1D HfC nanoribbons, we here simply adopted the κ_l of the monolayer HfC to evaluate the ZT value of the 1D HfC nanoribbons. In this regard, we neglect the phonon boundary scattering for the 1D system, which may further reduce κ_l. Nevertheless, the topological effects in the ZT optimization do not change since κ_l is considered independent from other parameters S, σ, and κ_e.

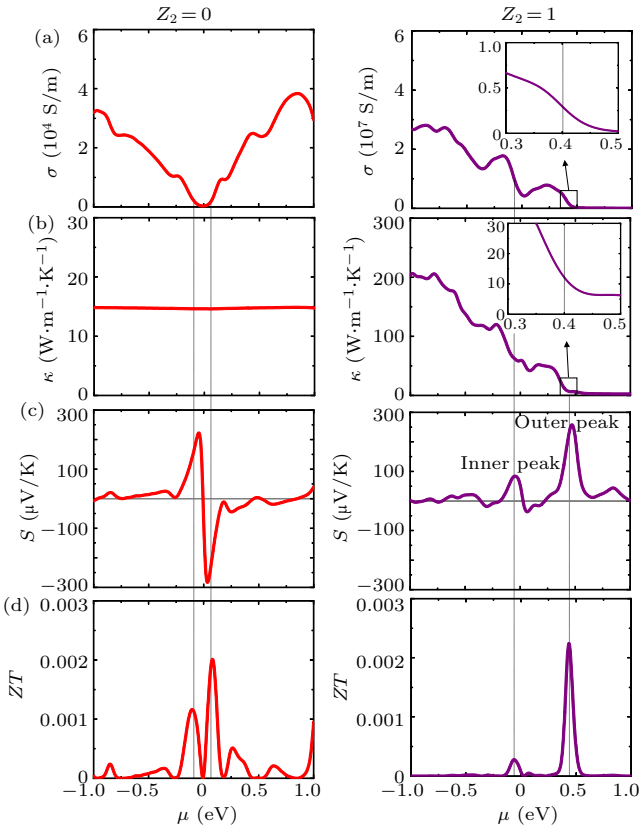


Fig. 3. TE properties of HfC nanoribbons. Chemical potential dependence of (a) electrical conductivity σ, (b) total thermal conductivity κ, (c) Seebeck coefficient S, and (d) dimensionless figure of merit ZT of both topological trivial phase (left) and non-trivial phase (right). Ribbon width and temperature were set as 35 cells and 300 K, respectively.

Seebeck coefficients S are shown in Fig. 3(c). In comparison with the trivial phase, which has an NSE, the optimized S values of the n-type ($\mu > 0$) and p-type ($\mu < 0$) are opposite in sign, the TI phase shows a characteristic of ASE that the

optimized S values have the same positive sign. We highlight the two pronounced S peaks on the right panel as the inner and outer peaks. The S peak around 0.0 eV of μ is denoted as the 'inner peak', which is inside the energy band of the edge states, the other peak around 0.4 eV as the 'outer peak', which lies at the band boundary of the edge states. It is worth emphasizing here that the S peaks of both TI and trivial phases share the same large magnitude, albeit from different origins. This is especially significant for the TI phase, which has concomitant decent electrical conductivity. As a result, the ZT peak values of the TI phase are higher by two to three orders of magnitude than that of the trivial phase, as shown in Fig. 3(d).

Next, we focus on how the ASE of the TI phase affects the TE properties of the HfC nanoribbons. It is essential to investigate separately the contributions of the edge and bulk states to the TE properties. The electrical conductivity and the Seebeck coefficient of the system are given by $\sigma = \sigma_e + \sigma_b$ and $S = (S_e\sigma_e + S_b\sigma_b)/\sigma$, see Appendix A3 for detail of the dual-channel model. In Fig. 4(a), we plot the contribution of bulk and edge states to the electrical conductivity, σ, as a function of chemical potential μ. For the case where $\mu < E_{boun}$, the edge states overlap with the bulk states, including the band gap, σ is dominated by the edge states. For the case where $\mu > E_{boun}$, that is, beyond the topological edge states, the bulk states take over the dominant role in contributing to the relevant property. Likewise, thermal conductivity κ in Fig. 4(b), mainly arising from carriers, shows a similar behavior.

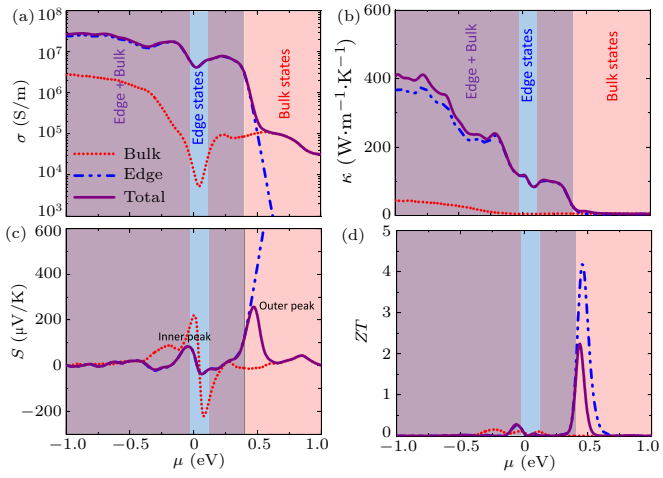


Fig. 4. (a)–(d) TE properties containing both edge and bulk components of topological non-trivial phase with ribbon width $N = 35$ cells at 300 K (N is the number of atoms). (a) The conductivity, (b) the thermal conductivity, (c) the Seebeck coefficient, (d) the ZT value.

ASE can be illustrated more clearly from both the separated and combined Seebeck coefficients as given in Fig. 4(c). For $\mu < E_{boun}$, though the bulk Seebeck coefficients S_b is relatively large, the total Seebeck coefficient S (the purple solid line) is almost equal to its edge counterpart S_e (the blue dashed line) due to the dominating electrical conductivity of the edge states, according to Eq. (A10). In this region, the Seebeck peaks occur at the valley of edge states ($\mu = -0.03$ eV and $+0.08$ eV), indicating the ASE characteristics. For $\mu > E_{boun}$, S_e monotonically increases with increasing μ, which fits well with the single-band model.[6] The compromise between the diverging S_e and the disappearing σ_e with increasing μ, gives rise to one more ASE or a pronounced S peak around 0.5 eV. With σ, κ, and S at hand in Figs. 4(a)–4(c), respectively, the total ZT is obtained and shown in Fig. 4(d). ZT exhibits the first peak (outer) at $\mu = 0.5$ eV and the second peak (inner) at $\mu = -0.1$ eV. The highest ZT value (~ 2.3) of the outer peak reveals the remarkable improvement of TE performance upon the bulk states by the ASE due to the topological edge states.

2.3. Size and temperature effects on thermoelectric properties

To further substantiate the TE performance augmented by topological states, the size effect, as one important factor proving the robustness of the TI properties, should be explored. HfC nanoribbons with ribbon width L varying from 56.72 Å to 132.27 Å were studied, and results are given in Fig. 5. As discussed above, the TI phase has a conductivity platform within the bulk gap derived by topological edge states, making it significantly different from the trivial phase, which has a conductivity valley in the band gap that dominates the evolution of Seebeck peaks. Thus, the dependence of Seebeck peaks on L is an important aspect that will help unveil the contribution of the edge states to S.

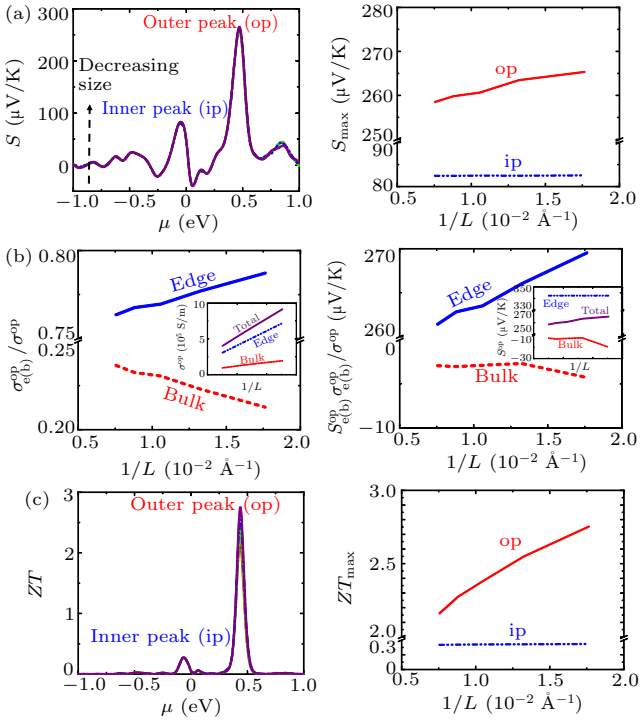


Fig. 5. Size dependence of TE performance: (a) S and (c) ZT of topological non-trivial phase as a function of μ and size $1/L$. The right panels of (a) and (c) are the maximal values of S and ZT for both inner and outer peaks, as defined by dashed lines on the left panel. (b) The weight of the edge and bulk states contributed to electrical conductivity and Seebeck coefficient for the outer peak (op). Here $\sigma^{op} = \sigma_e^{op} + \sigma_b^{op}$, $S^{op} = (S_e^{op}\sigma_e^{op} + S_b^{op}\sigma_b^{op})/\sigma^{op}$.

As shown in Fig. 5(a), the peak position (chemical potential μ) of S of both inner (ip) and outer peaks (op) remains unchanged when changing L. But the maximum value $S_{\max}$ of the outer peak increases with decreasing L, while the $S_{\max}$ of the inner peak is independent of L and shows its stability ($S_{\max} \sim 85$ μV/K). This can be attributed to their different origins, i.e., the inner peak arises dominantly from the topological edge states, while the outer peak results from the interplay of edge and bulk states. Equation (A10) in Appendix A shows that the contribution weight of both edge and bulk states to Seebeck coefficient S can be determined by their electrical conductivity σ. Now, for the outer Seebeck peak, the weight of the edge states, as evaluated by the ratio of the edge conductivity $\sigma_{\mathrm{e}}^{\mathrm{op}}$ to total conductivity σ^{op} as given on the left panel of Fig. 5(b), increases with decreasing L. Therefore, the weight of edge states contributed to the total S shall increase, as shown on the right panel of Fig. 5(b). In Fig. 5(c), ZT and $ZT_{\max}$ as a function of μ and L at 300 K, respectively, show the similar behavior of S.

Temperature effects on the TE properties of the TI phase are also investigated. S and ZT of HfC nanoribbons are calculated as a function of the temperatures T and chemical potential μ, as shown in Figs. 6(a) and 6(b). The response to thermal fluctuation of the TI phase is somewhat complicated due to the existence of topological edge states. It can be analyzed from three aspects: peak position, peak value, and peak shape. The first is the peak position. As temperature increases, the outer peak tends to shift away from edge states while the inner peak hardly shifts. As for peak value, despite a slight fall below 400 K, the outer peak tends to grow with temperature, while the inner peak rises and falls as temperature increases. This is partly due to the decreasing trend of $S_{\mathrm{b}}\sigma_{\mathrm{b}}$ as temperature increases. Regarding peak shape, both the inner and outer peaks show thermal broadening, which is similar to the normal Seebeck effect. As shown on the right side of Fig. 6, ZT of the TI phase shows similar behavior to that of the Seebeck coefficient, except that the ZT outer peak keeps going up with increasing temperature, largely because of the persistent dropping of phonon conductivity with temperature.

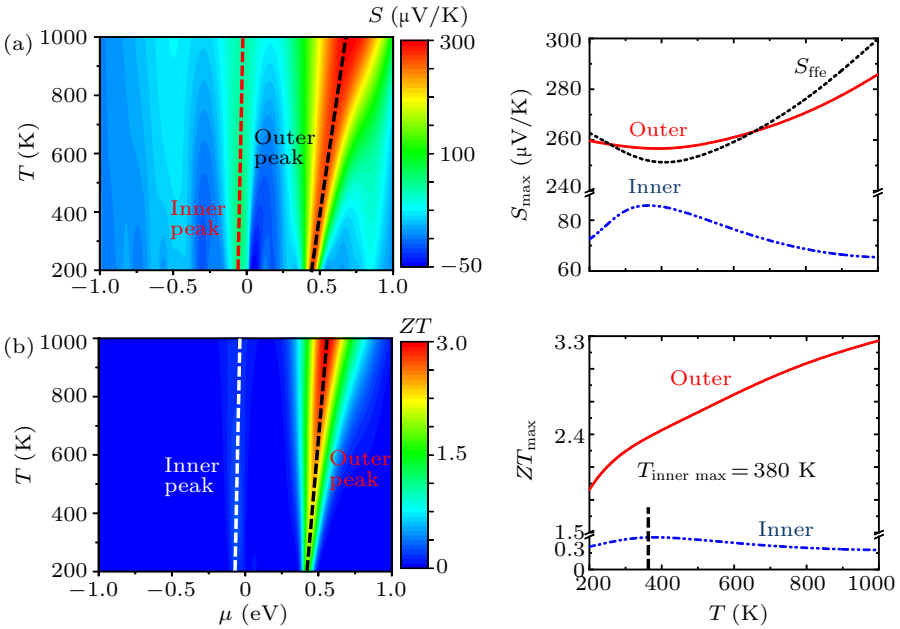


Fig. 6. Peak evolution of (a) S and (b) ZT of topological non-trivial phases under the change of temperature T and chemical potential μ. The left-hand side shows peak positions, while the right-hand side shows peak values.

3. Conclusion

The TE properties of the HfC monolayer are investigated by the first-principles calculations and analytical approach. Our results reveal that the ASE in the HfC monolayer can significantly improve the TE performance by at least one order of magnitude when HfC is transformed from the trivial phase to the Z_2 TI phase by strain. The ASE of the Z_2 TI phase is found to give two main peaks of the Seebeck coefficient. The first peak (or inner peak) has $S_{\max}$ up to ~ 100 μV/K and is independent of the width L of the HfC nanoribbon. The second peak (or outer peak) is the result of competition between bulk and edge states. Thus, the outer peak has $S_{\max}$ up to ~ 290 μV/K and sensitively dependent on the width L and temperature T. As a consequence, L and T can be used to optimize the ZT value (up to 2–3) at the outer peak. Furthermore, we also calculate the lattice thermal conductivity κ_{l} of two phases in HfC. κ_{l} of the Z_2 TI phase is much lower than that of the trivial phase, leading to further enhancement of the thermoelectric properties of the Z_2 TI phase.

Appendix A. Calculations

A1. Electronic band structure and topological property calculations

The electronic band structure of the HfC monolayer was calculated based on density functional theory (DFT) as implemented in the Vienna *ab initio* simulation package (VASP).[22] Projector augmented wave (PAW) pseudopotentials with a plane-wave cutoff energy of 500 eV were used to describe electron–ion interaction.[23] We used the Perdew–Burke–Ernzerhof (PBE) form of the exchange–correlation functional in the generalized gradient approximation (GGA).[24] Two types of self-consistent DFT calculations were performed in this work, namely, standard self-consistent field (SCF) calculation with $\boldsymbol{k}$-mesh of 10^{-2} Å^{-1} and high-accuracy SCF calculation with $\boldsymbol{k}$-mesh of 5×10^{-3} Å^{-1}. The spin–orbit coupling (SOC)[25] was fully accounted for in the electronic calculation. To investigate topological edge-state properties, the WANNIER90 code[26] was used to obtain the effective tight-binding Hamiltonian. Electronic transport properties of the material were calculated by solving the semi-classical Boltzmann transport equation[27] with more details given in Appendix A2.

A2. Electrical transport and thermoelectric properties calculation

By solving the linearized Boltzmann equations within the relaxation time approximation, the electrical conductivity σ, electronic thermal conductivity $\kappa_{\rm e}$, and Seebeck coefficient S, are given by[1]

$$\sigma^{\alpha\beta} = e^2 K_0^{\alpha\beta}, \tag{A1}$$

$$\kappa_{\rm e}^{\alpha\beta} = \frac{1}{T}\left(K_2^{\alpha\beta} - \frac{(K_1^{\alpha\beta})^2}{K_0^{\alpha\beta}}\right), \tag{A2}$$

$$S^{\alpha\beta} = -\frac{K_1^{\alpha\beta}}{eTK_0^{\alpha\beta}}, \tag{A3}$$

respectively, where α, β $(=x,y,z)$ is the direction of electrical transport, $K_n^{\alpha\beta}$ $(n=0,\,1,\,2)$ is a general transport integral, which is defined as

$$K_n^{\alpha\beta} = \int \mathcal{G}^{\alpha\beta}(E-\mu)^n\left(-\frac{\partial f_{\rm F}}{\partial E}\right){\rm d}E, \tag{A4}$$

where E is the energy of electron, μ is the chemical potential, $f_{\rm F} = \left[{\rm e}^{(E-\mu)/k_{\rm B}T}+1\right]^{-1}$ is the Fermi–Dirac distribution function, and $\mathcal{G}$ is the transport distribution function, and in the band theory is given by

$$\mathcal{G}^{\alpha\beta} = \frac{1}{V}\sum_{i,\boldsymbol{k}} v_{i,\boldsymbol{k}}^{\alpha} v_{i,\boldsymbol{k}}^{\beta} \tau_{i,\boldsymbol{k}} \delta(E-E_{i,\boldsymbol{k}}), \tag{A5}$$

where V is the unit-cell volume, $\tau_{i,\boldsymbol{k}}$ is the relaxation time, $v_{i,\boldsymbol{k}}^{\alpha} = \hbar^{-1}\partial E_{i,\boldsymbol{k}}/\partial k_{\alpha}$ is the group velocity, $\boldsymbol{k}$ is the wavevector, and i is the band index of electron.

Table A1. Coefficients of 1D ribbons at the bulk band edges within the relaxation time approximation.

Z_2	$\tau_{\rm p}\sqrt{T}$ (fs·K$^{1/2}$)	$\tau_{\rm n}\sqrt{T}$ (fs·K$^{1/2}$)	$m_{\rm p}^*$ ($m_{\rm e}$)	$m_{\rm n}^*$ ($m_{\rm e}$)	$E_{1\rm p}$ (eV)	$E_{1\rm n}$ (eV)
0	159.55	161.92	0.22	0.09	6.84	8.39
1	7.45	21.19	0.91	0.69	22.15	14.04

In order to take topological edge states into consideration, the dual scattering time (DST) model[28] is adopted for TIs, and the transport integral can be written as

$$K_n^{\alpha\beta} = K_n^{\alpha\beta}(\tau_{\rm bulk}) + K_n^{\alpha\beta}(\tau_{\rm edge}), \tag{A6}$$

in which $\tau_{\rm bulk(edge)}$ denotes the relaxation time of bulk (edge) states. Taking constant relaxation time approximation, we can calculate the relaxation time of the system via the deformation potential (DP) theory,[21] in which the relaxation time of a one-dimensional system can be calculated by[29]

$$\tau_{\rm p(n)} = \sqrt{\frac{2}{\pi}}\frac{\hbar^2 C}{\sqrt{k_{\rm B}Tm_{\rm p(n)}^*}\Xi_{\rm p(n)}^2}, \tag{A7}$$

where p (n) refers to the p-type (n-type) of the carrier, $C = \frac{2}{l_0}\frac{\partial^2 E}{\partial u^2}$ is the 1D strain modulus, where $u = \Delta l/l_0$ is strain along the periodic direction, $m_{\rm p(n)}^*$ is the effective mass of p-type (or n-type) carrier, $\Xi_{\rm p(n)} = \partial E_{\rm p(n)}/\partial u$ is the deformation potential, where $E_{\rm p(n)}$ is the energy value of band edge of either the conduction band minimum (CBM) or the valence band maximum (VBM) with respect to the vacuum level.

Note that equation (A7) works properly only in the vicinity of the band edge (for example, near VBM or CBM). Moreover, to further explore the transport properties with the topological edge states involved, it is not proper anymore to consider chemical potential-independent constant relaxation time τ. Recently, a method, that was successfully applied to the investigation of nodal-line semimetal,[30,31] considers the dependence of relaxation time on the density of states (DOS) and has the relaxation time expressed as

$$\tau_{\rm p(n)}(E) = \frac{\zeta_{\rm p(n)}}{D_{\rm p(n)}(E)}, \tag{A8}$$

where $D_{\rm p(n)}(E)$ and $\zeta_{\rm p(n)}$ represent the DOS and an energy-independent constant of the p-type (or n-type) carrier, respectively. $\zeta_{\rm p(n)}$ is to be determined at VBM or CBM by Eq. (A7). In our case, $\zeta_{\rm p0(1)} = 1.89\times10^{-13}$ (2.62×10^{-13}) s/eV and $\zeta_{\rm n0(1)} = 7.87\times10^{-13}(8.86\times10^{-14})$ s/eV, with '0' and '1' representing the unstrained and strained structures with the Z_2 topological invariant of 0 and 1, respectively. The relaxation time of the topological edge state is expected to be much higher than that of the bulk state, for example, $\tau_{\rm edge} \cong 100\tau_{\rm bulk}$, which works at band edges for most of TIs.[32–34] Here, we consequently adopt $\tau_{\rm edge} = 100\tau_{\rm bulk}$ at the band edge of the bulk states throughout this work.

A3. Dual-channel model

The electrical conductivity of ASE in TIs can be described via a dual-channel model with one channel for edge states and another for bulk states, according to Eqs. (A6) and (A1), the total conductivity is given by

$$\sigma = \sigma_{\mathrm{e}} + \sigma_{\mathrm{b}}, \tag{A9}$$

and thus, according to Eq. (A3), the total Seebeck coefficient can be given by[15]

$$S = \frac{S_{\mathrm{e}}\sigma_{\mathrm{e}} + S_{\mathrm{b}}\sigma_{\mathrm{b}}}{\sigma_{\mathrm{e}} + \sigma_{\mathrm{b}}}, \tag{A10}$$

where $S_{\mathrm{e(b)}}$ and $\sigma_{\mathrm{e(b)}}$ denote the Seebeck coefficient and electrical conductivity of edge (bulk) states, respectively. In the relaxation time approximation (RTA), the two channels were distinguished by applying different relaxation time on them, which is called the dual scattering time (DST) model.[15] By using the tight-binding method, Gaffar *et al.*[17] calculated S of bismuthene, and they found the ASE in the topological phase of bismuthene that leads to enhancement of the ZT value. The ASE has also been observed in an experiment in 2D TI ultrathin Bi_2Te_3 film.[35,36]

A4. Phonon dispersion relation, thermal conductivity, and topological band properties

The phonon band structure and its transport property of the system were investigated based on DFT and Boltzmann transport theory, as shown in Fig. A1. Phonon dispersion relation was calculated with the finite displacement method as implemented in the PHONOPY code.[37] $5\times5\times1$ supercell was selected with radius cut-off of 5 Å. The lattice thermal conductivity κ_{l}, which is usually evaluated by the phonon lifetime, was self-consistently calculated in the ShengBTE package.[38] The second-order harmonic inter-atomic force constants (IFCs) were calculated by the PHONOPY package, and the third-order anharmonic IFCs were evaluated by using a $5\times5\times1$ supercell and up to the fifth-nearest neighbors considered by ShengBTE.

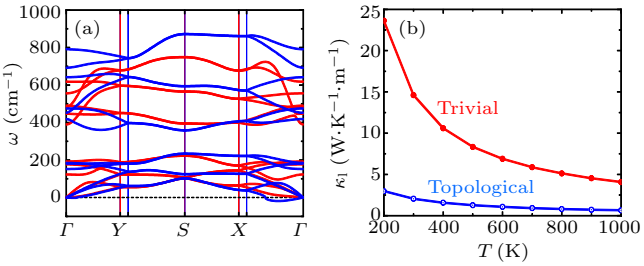


Fig. A1. (a) The phonon spectrum of HfC monolayer, with no negative frequencies for the original structure, ensuring dynamical stability of the system, despite there are some states with minute negative frequencies exist in the strained case, it is acceptable for lattice dynamical analyzing. (b) The lattice thermal conductivity of HfC monolayer, showing a decreasing tendency as temperature increases.

The electron band structure of tight-binding Wannier Hamiltonian fits well with DFT result, as shown in the following Fig. A2.

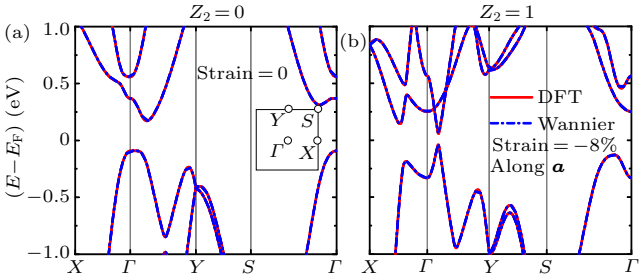


Fig. A2. DFT calculated band structure (red lines) and corresponding results obtained from a TB model (blue dot-dash lines), showing a nice goodness of fit around Fermi level. Panels (a) and (b) for trivial phase and TI phase, respectively. From which one can verify the reliability of the TB model.

By using Wanniertools, we confirmed the topological property and the edge states of the strained HfC, as shown in Fig. A3.

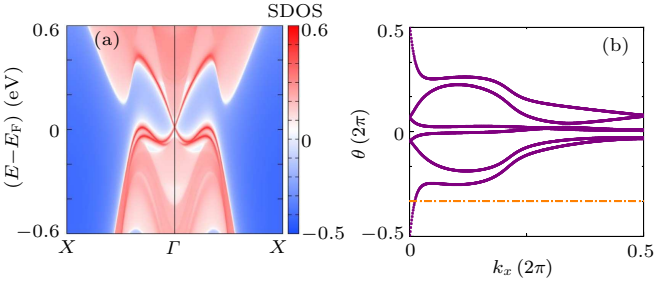


Fig. A3. (a) The edge density of states of HfC Z_2 topological phase under the open boundary condition, (b) the Wilson loop of Wannier centers of HfC monolayer under strain of -8% along a direction, the evolution lines cross the reference line an odd number of times in the $k_z=0$ plane, indicating the nontrivial Z_2 topological property of the system.

A5. Elastic stability and thermodynamic stability

To further verify the stability of the HfC monolayer, we introduced an elastic stability analyze. For a 2D orthorhombic lattice, the stiffness matrix can be given as follows:

$$C = \begin{bmatrix} C_{11} & C_{12} & C_{13} & & & \\ \cdot & C_{22} & C_{23} & & & \\ \cdot & \cdot & C_{33} & & & \\ & & & C_{44} & & \\ & & & & C_{55} & \\ & & & & & C_{66} \end{bmatrix}, \tag{A11}$$

where $C_{\mu\nu} = \frac{1}{V_0}\frac{\partial^2 E}{\partial u_\mu \partial u_\nu}$ is the elastic tensor. To meet the necessary and sufficient Born criteria, one will have[39]

$$\begin{aligned} &C_{11}>0, \quad C_{11}C_{22}>{C_{12}}^2, \\ &C_{11}C_{22}C_{33}+2C_{12}C_{13}C_{23}>C_{11}{C_{23}}^2+C_{22}{C_{13}}^2+C_{33}{C_{12}}^2, \\ &C_{44}>0, \quad C_{55}>0, \quad C_{66}>0. \end{aligned} \tag{A12}$$

Here, in the HfC monolayer case, $C_{11}=44.840$ GPa, $C_{22}=102.922$ GPa, $C_{33}=3.145$ GPa, $C_{12}=14.106$ GPa, $C_{13}=7.553$ GPa, $C_{23}=3.264$ GPa, $C_{44}=4.362$ GPa, $C_{55}=5.018$ GPa, $C_{66}=29.356$ GPa, which satisfies the necessary and sufficient Born criteria.

Despite the thermodynamic stability has already been investigated in previous work, we supplement the energy evolution of the *ab initio* molecular dynamics (AIMD) simulation of both original structure and the structure under strain, as shown in Fig. A4, the snapshot of the structures at different phases of AIMD simulation is demonstrated in Fig. A5. The chosen ensemble is the NVT ensemble, the time span is set as 5 ps.

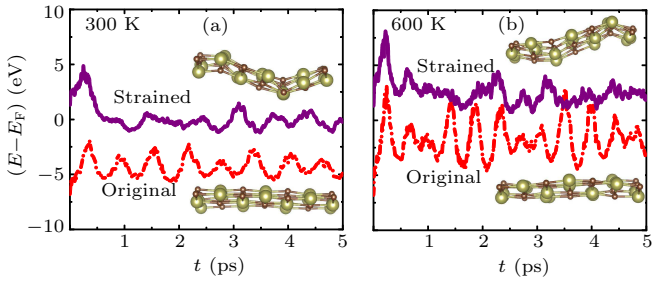


Fig. A4. The energy evolution during AIMD: (a) under the temperature of 300 K and (b) under the temperature of 600 K, with $E_0 = -595$ eV.

Here we make a brief discussion on preparing HfC monolayer material in experiment. First, the intrinsic HfC monolayer exhibits a phonon spectrum with no obvious negative in Fig. A1. Second, although some small negative frequency appears in the out-of-plane flexual mode under -8% strain, it can be easily suppressed by lattice anharmonicity at high working temperature. Third, the atomic structure can remain intact up to 600 K for as long as a few picoseconds, as shown in Figs. A4 and A5, indicating that the monolayer structure is thermodynamically and dynamically stable and can be prepared in experiment.

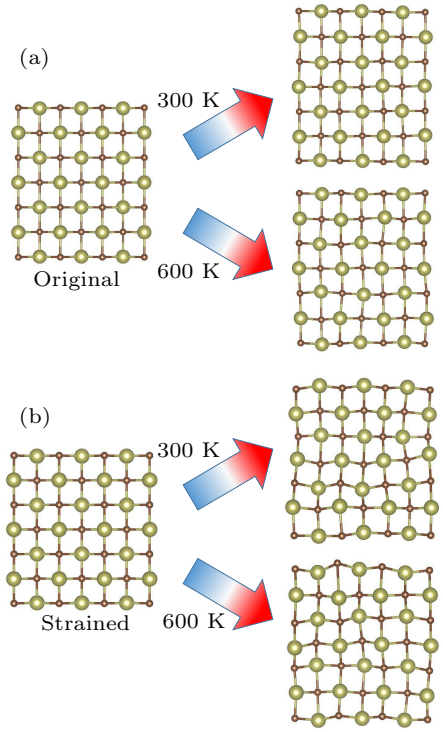


Fig. A5. The snapshot of the initial structures on the left-hand side, and the final structures at 5 ps of AIMD simulation on the right: (a) for the original case and (b) for the strained case.

Acknowledgments

Project supported by the National Natural Science Foundation of China (Grant No. 52031014), the Strategic Priority Research Program of the Chinese Academy of Sciences (Grant No. XDB0460000), and the National Key Research and Development Program of China (Grant No. 2022YFA1203900). Baojuan Dong acknowledges the National Natural Science Foundation of China (Grant Nos. 12004228 and U21A6004). Riichiro Saito acknowledges a JSPS KAKENHI (Grant No. JP22H00283), Nguyen Tuan Hung acknowledges financial support from the Frontier Research Institute for Interdisciplinary Sciences, Tohoku University. Weijiang Gong acknowledges financial support from the National Natural Science Foundation of China (Grant No. 51702146). The simulation work was carried out at the National Supercomputer Center in Tianjin, China, and the calculations were performed on TianHe-1(A). Special thanks to professor Dr. Shaoqing Wang, who once guided Wenlai Mu during his lifetime.

References

[1] Goldsmid H J *et al.* 2010 *Introduction of Thermoelectricity* (Heidelberg, Germany: CRC press)
[2] Rowe D M E 1995 *CRC Handbook of Termoelectrics* (Springer)
[3] Pei Y, Shi X, LaLonde A, Wang H, Chen L and Snyder G J 2011 *Nature* **473** 66
[4] Zhu H, Zhang B, Wang G, Peng K, Yan Y, Zhang Q, Han X, Wang G, Lu X and Zhou X 2019 *J. Mater. Chem. A* **7** 11690
[5] Hung N T, Hasdeo E H, Nugraha A R T, Dresselhaus M S and Saito R 2016 *Phys. Rev. Lett.* **117** 036602
[6] Hung N T, Nugraha A R T, Hasdeo E H, Dresselhaus M S and Saito R 2015 *Phys. Rev. B* **92** 165426
[7] Gong Y, Zhang S, Hou Y, Li S, Wang C, Xiong W, Zhang Q, Miao X, Liu J, Cao Y, Li D, Chen G and Tang G 2023 *ACS Nano* **17** 801
[8] Tao P, Guo H H, Yang T and Zhang Z D 2014 *Chin. Phys. B* **23** 106801
[9] Guo H H, Yang T, Tao T and Zhang Z D 2014 *Chin. Phys. B* **23** 017201
[10] Song H D, Sheng D, Wang A Q, Li J G, Yu D P and Liao Z M 2017 *Chin. Phys. B* **26** 037301
[11] Qi X L and Zhang S C 2010 *Phys. Today* **63** 33
[12] Hasan M Z and Kane C L 2010 *Rev. Mod. Phys.* **82** 3045
[13] Sun Y, Chen X Q, Yunoki S, Li D and Li Y 2010 *Phys. Rev. Lett.* **105** 216406
[14] Dong Q X, Ruan B B, Huang Y F, Wang Y Y, Zhang L B, Bai J L, Liu Q Y, Cheng J W, Ren Z A and Chen G F 2023 *Chin. Phys. B* **32** 066501
[15] Xu Y, Gan Z and Zhang S C 2014 *Phys. Rev. Lett.* **112** 226801
[16] Hasdeo E H, Krisna L, Hanna M Y, Gunara B E, Hung N T and Nugraha A R T 2019 *J. Appl. Phys.* **126** 036602
[17] Gaffar M, Wella S A and Hasdeo E H 2021 *Phys. Rev. B* **104** 205105
[18] Takahashi R and Murakami S 2010 *Phys. Rev. B* **81** 161302(R)
[19] Zhang R W, Ji W X, Zhang C W, Li S S, Li P and Wang P J 2016 *J. Mater. Chem. C* **4** 2088
[20] Zhou L J, Shao B, Shi W J, Sun Y, Felser C, Yan B H and Frauenheim T 2016 *2D Mater.* **3** 035022
[21] Bardeen J and Shockley W 1950 *Phys. Rev.* **80** 72
[22] Kresse G and Furthmuller J 1996 *Phys. Rev. B* **54** 11169
[23] Kresse G and Joubert D 1999 *Phys. Rev. B* **59** 1758
[24] Blöchl P 1994 *Phys. Rev. B* **50** 17953
[25] Wang S K, Pratama F R, Ukhtary M S and Saito R 2020 *Phys. Rev. B* **101** 081414(R)
[26] Mostofi A A, Yates J R, Lee Y S, Souza I, Vanderbilt D and Marzari N 2008 *Comput. Phys. Commun.* **178** 685
[27] Madsen G K H and Singh D J 2006 *Comput. Phys. Commun.* **175** 67

[28] Gooth J, Gluschke J G, Zierold R, Leijnse M, Linke H and Nielsch K 2015 *Semicond. Sci. Technol.* **30** 015015
[29] Beleznay F, Bogár F and Ladik J 2003 *J. Chem. Phys.* **119** 5690
[30] Hung N T, Nugraha A R T and Saito R 2018 *Phys. Rev. Appl.* **9** 024019
[31] Hung N T, Adhidewata J M, Nugraha A R T and Saito R 2022 *Phys. Rev. B* **105** 115142
[32] Muller G, Weiss D, Khaetskii A, Vonklitzing K, Koch S, Nickel H, Schlapp W and Losch R 1992 *Phys. Rev. B* **45** 3932
[33] Daumer V, Golombek I, Gbordzoe M, Novik E, Hock V, Becker C, Buhmann H and Molenkamp L 2003 *Appl. Phys. Lett.* **83** 1376
[34] Wang T H and Jeng H T 2018 *ACS Appl. Energy Mater.* **1** 5646
[35] Ahmad M, Agarwal K and Mehta B 2020 *J. Appl. Phys.* **128** 035108
[36] Matsushita S Y, Huynh K K, Yoshino H, Tu N H, Tanabe Y and Tanigaki K 2017 *Phys. Rev. Mater.* **1** 054202
[37] Togo A, Oba F and Tanaka I 2008 *Phys. Rev. B* **78** 134106
[38] Li W, Carrete J, Katcho N A and Mingo N 2014 *Comput. Phys. Commun.* **185** 1747
[39] Mouhat F and Coudert F X 2014 *Phys. Rev. B* **90** 224104